

Certified Coil Geometry Learning for Short-Range Magnetic Actuation and Spacecraft Docking Application

Yuta Takahashi^{1,2}, Hayate Tajima³, Shin-ichiro Sakai⁴

Abstract—This paper presents a learning-based framework for approximating an exact magnetic-field interaction model, supported by both numerical and experimental validation. High-fidelity magnetic-field interaction modeling is essential for achieving exceptional accuracy and responsiveness across a wide range of fields, including transportation, energy systems, medicine, biomedical robotics, and aerospace robotics. In aerospace engineering, magnetic actuation has been investigated as a fuel-free solution for multi-satellite attitude and formation control. Although the exact magnetic field can be computed from the Biot–Savart law, the associated computational cost is prohibitive, and prior studies have therefore relied on dipole approximations to improve efficiency. However, these approximations lose accuracy during proximity operations, leading to unstable behavior and even collisions. To address this limitation, we develop a learning-based approximation framework that faithfully reproduces the exact field while dramatically reducing computational cost. The proposed method additionally provides a certified error bound, derived from the number of training samples, ensuring reliable prediction accuracy. The learned model can also accommodate interactions between coils of different sizes through appropriate geometric transformations, without retraining. To verify the effectiveness of the proposed framework under challenging conditions, a spacecraft docking scenario is examined through both numerical simulations and experimental validation.

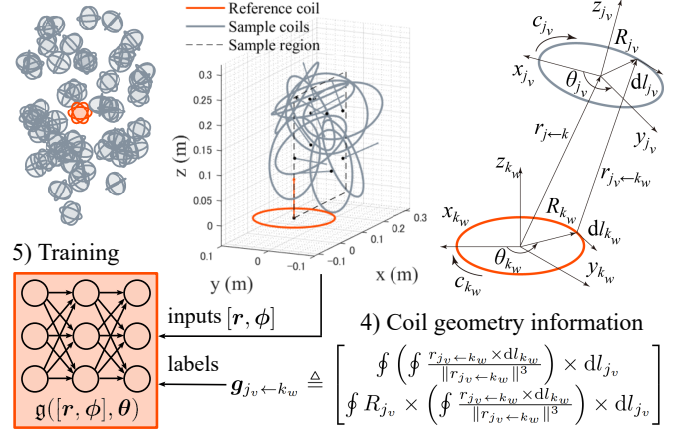
Index Terms—Supervised Learning, Robotics Control, Spacecraft Docking, Electromagnetic Formation Flight.

I. INTRODUCTION

EXACT magnetic-field interaction modeling plays a central role across diverse domains that require high accuracy and responsiveness. In transportation and infrastructure, it supports linear motors and maglev systems by coordinating propulsion, levitation, and guidance. The energy sector likewise depends on precise inductance estimation for wireless power transfer, drawing on analytical formulations [1]. In medicine, triaxial coil systems enable multichannel transcranial magnetic stimulation, enhancing the spatial selectivity of neural excitation [2]. Beyond this, magnetic fields have been used in biomedical robotics to steer microrobots through internal organs, facilitating targeted drug delivery and minimally invasive procedures [3]. In the aerospace sector, the Earth’s magnetic environment has been exploited for spacecraft attitude control using magnetorquers (MTQs). Conventional

Offline: Coil geometry calculation for coils of radius a_{NN}

1) Rand. coils 2) Coordinate transformation 3) Circular integration



Online: Formation and attitude control for coils of radius $a_{inf} = \gamma a_{NN}$

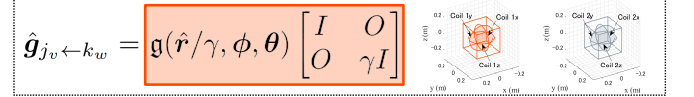


Fig. 1: Coil geometry learning to predict the magnetic interaction.

actuators, such as thrusters, generate a plume, which causes sensor contamination and disturbance in proximity operations. In contrast, magnetic-field interaction control mitigates these issues, enhancing mission flexibility and longevity. Several studies apply this actuation to the proximity operations, including non-contact micro-vibration suppression [4], debris removal [5], formation keeping [6], and satellite docking [7], [8]. These highlight magnetic-field modeling as a unifying technology for control, sensing, and actuation.

The aerospace community has been an active field in developing a theoretical framework for controlling magnetic-field interactions to achieve multiple objectives. Previous studies have considered magnetic-field interactions in space to control the relative positions of various satellites with extremely high precision. They are referred to as electromagnetic formation flight [8]–[14] with demonstrations on the International Space Station [9]. Since this system is naturally underactuated for swarm control [12], previous studies extend controllability through time-integrated current control, such as the alternating current (AC) method [12], [14]. Recent studies investigate the six-degree-of-freedom control of a large number of satellites through AC control [12] and demonstration [13] with a learning-aided technique [15]. These lead to a new class of commercial and scientific missions, such as the fuel-free on-orbit construction of space structures [16].

However, the conventional magnetic interaction model is invalid for short-range interactions, and predicting the ex-

¹Graduate Student, Department of Mechanical Engineering, Tokyo Institute of Technology, Ookayama Meguro, Tokyo 152-8552, Japantakahashi.y.cl@m.titech.ac.jp

²Researcher, Satellite Research and Development, Interstellar Technologies Inc., 149-7 Hiroo, Hokkaido 089-2113, Japan

³Graduate Student, Department of Advanced Energy, The University of Tokyo, 5-1-5 Kashiwanoha, Kashiwa, Chiba 277-8561, Japan

⁴Professor, Department of Spacecraft Engineering, Japan Aerospace Exploration Agency, 3-1-1 Yoshinodai, Sagami-hara, Kanagawa 252-5210, Japan

act interaction is impractical in real-time due to the high computational burden. The exact magnetic interaction model developed for formation control [11] includes the double circular integration using coil geometry and the relative coil states. This is calculated based on the Biot–Savart law, and the associated computational cost is prohibitive. To avoid its cost, existing research primarily uses the far-field approximation [11], assuming that the distance between coils is significantly greater than the coil radius. While this model reduces computational cost, it becomes less accurate as the distance between the coils decreases. Consequently, the desired control cannot be achieved at short distances without proper strategy, leading to inaccuracies, instability, and, in the worst case, satellite collision [8]. Therefore, real-time calculations were always a trade-off between accuracy and computational time.

To this end, this study proposes a learning-based framework to predict the exact magnetic field interaction with the certified model error bound. The effectiveness of our approaches is demonstrated through numerical and experimental methods in the context of docking. For these validations, we apply our learning framework to a decentralized current allocation without inter-agent communication, extending the far-field model strategy [15]. The overall structure of our study is as follows: Section II formulates a multilayer perceptron model and the exact magnetic model of a one-axis coil to prepare for the derivation of our framework. Section III derives an interaction model using a three-axis coil referred to as “coil geometry information” and a communication-free decentralized current calculation for the exact magnetic-field model. Finally, our learning-based coil-specific geometry modeling framework is presented in Section IV, along with generalization methods for arbitrary coil radius and error-bound certification. Section V conducts the offline training and validates the proposed learning-based current calculation for satellite docking by numerical simulations and experimental comparison with the conventional approximation model.

II. PRELIMINARIES

This section introduces the magnetic field interaction model for multi-agent control as preliminaries. Our mathematical notation about vector and coordination are follow: $\{\mathbf{a}\}$ is defined as basis vector of an arbitrary frame (A) such that $\{\mathbf{a}\} = \{\mathbf{a}_x^T, \mathbf{a}_y^T, \mathbf{a}_z^T\}^T$ and we define a_p component of an arbitrary vector $\mathbf{p} \in \mathbb{R}^3$ in this frame, i.e., $\mathbf{p} = \{\mathbf{a}\}^T a_p = \{\mathbf{b}\}^T b_p = \{\mathbf{b}\}^T C^{B/A} a_p$ where $C^{B/A} \in \mathbb{R}^{3 \times 3}$ is the coordinate transformation matrix from frame (A) to (B). We define the Lipschitz constant $\|f\|_{\text{Lip}}$ for a general differentiable function f as $\forall x_1, x_2 : \|f(x_1) - f(x_2)\|_2 / \|x_1 - x_2\|_2 \leq \|f\|_{\text{Lip}} = \sup_x \sigma(\nabla f(x))$ and $\|f_1 \circ f_2\|_{\text{Lip}} \leq \|f_1\|_{\text{Lip}} \|f_2\|_{\text{Lip}}$.

A. Multilayer Perceptron Model and Error Bound

This subsection introduces the conservative error bound between true value and approximation values generated by the Multilayer Perceptron (MLP) model. The MLP represents the functional mapping from inputs x into outputs $\mathbf{g}_{(\mathbf{x}^{(j)}, \theta)}$ such as a $(L+1)$ -layer neural network:

$$\mathbf{g}_{(\mathbf{x}^{(j)}, \theta)} = W^{(L+1)} \phi(\dots \phi(W^{(1)} X^{(j)} + b^{(1)}) \dots) + b^{(L+1)}$$

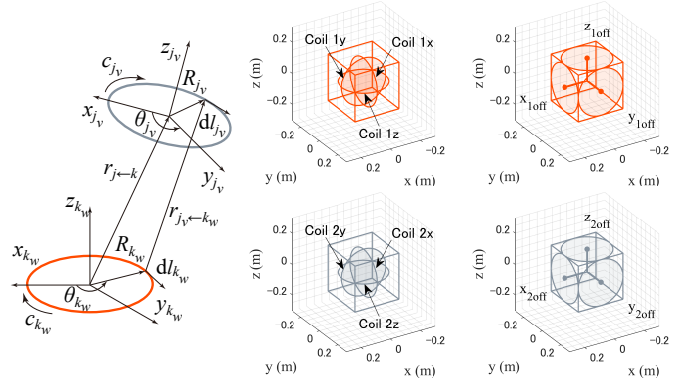


Fig. 2: The definition of circulant integration in Eq. (3) and the coil model of target and chaser with offset in subsection III-A.

where the activation function $\phi(\cdot)$ and the MLP parameters θ include the weights $\theta_w = W^{(1)}, \dots, W^{(L+1)}$, and the bias $\theta_b = b^{(1)}, \dots, b^{(L+1)}$. Since the spectral norm of each layer is $\|W^{(l)} \mathbf{x} + b^{(l)}\|_{\text{Lip}} = \sup_{\mathbf{x}} \sigma(\nabla(W^{(l)} \mathbf{x} + b^{(l)})) = \sigma(W^{(l)})$, $\|g\|_{\text{Lip}}$ is bounded as $\|g\|_{\text{Lip}} \leq \|\phi\|_{\text{Lip}} \prod_{l=1}^{L+1} \sigma(W^{(l)})$ [17]. Then, we obtain the Lipschitz constant of the error function $e_{g/g(x)} = \|g_x - \mathbf{g}_x\|$ as $(L_g + L_g)$ since we have

$$\|e_{g/g(x)} - e_{g/g(y)}\| = \|(g_x - g_y) - (\mathbf{g}_x - \mathbf{g}_y)\| \leq (L_g + L_g) \|x - y\|$$

where the Lipschitz constants L_g for the true function and L_g for the MLP model. The upper bound of learning error, i.e., $\sup_{x \in \mathcal{X}} \|g_x - \mathbf{g}_x\|$, for a compact set \mathcal{S}_R is bounded as

$$\sup_{x \in \mathcal{S}_R} \|g_x - \mathbf{g}_x\| \leq \sup_{x' \in \mathcal{T}_R} \|g_{x'} - \mathbf{g}_{x'}\| + (L_g + L_g) \rho_{\mathcal{S}_R} \quad (1)$$

where the covering radius $\rho_{\mathcal{S}_R} = \sup_{x \in \mathcal{S}_R} \min_{x' \in \mathcal{T}_R} \|x - x'\|$.

B. Electromagnetic Interaction Model of One-Axis Coil

This subsection derives the magnetically interacting model between one-axis coils. We model the k th one-axis coil as a circular air-core coil and define its dipole moment as $\mu_k = N_t A c_k \mathbf{n}$ where the number of coil turns N_t , the area enclosed by the coil $A = \pi a_k^2$ with the coil radius a_k , the current strength $c_k(t)$, and \mathbf{n} is the unit vector perpendicular to the plane of the coil. The exact magnetic field model $B(r_{j \leftarrow k})$ [11] using the well-known Biot-Savart law is

$$B(r_{j \leftarrow k}) = \frac{\mu_0 c_k}{4\pi} \oint \frac{dl_k \times r_{j \leftarrow k w}(\theta_{j \leftarrow k w})}{\|r_{j \leftarrow k w}(\theta_{j \leftarrow k w})\|^3} \in \mathbb{R}^3$$

where the magnetic permeability μ_0 , the coil element $dl_k \in \mathbb{R}^3$, and the distance between coil elements $r_{j \leftarrow k w}(\theta_{j \leftarrow k w}) = r_{j \leftarrow k} + C^{k/j} R_j - R_k$, the coil radius vector $R_k(\varphi) = a_k [\cos \varphi, \sin \varphi, 0]^T$, the k th coil element vector $dl_k(\varphi) = (dR_k(\varphi)/d\varphi) d\varphi$. The electromagnetic force and torque experienced by the j th one-axis coil due to the magnetic field generated by the k th one-axis coil $u_{j \leftarrow k}^{\text{axis}} = [f_{j \leftarrow k}; \tau_{j \leftarrow k}]$ are

$$u_{j \leftarrow k}^{\text{axis}} = \frac{\mu_0 \mu_k \mu_j}{4\pi A^2} \begin{bmatrix} \int_{\theta_j=0}^{\theta_j=2\pi} \int_{\theta_k=0}^{\theta_k=2\pi} \frac{r_{j \leftarrow k w} \times dl_k}{\|r_{j \leftarrow k w}\|^3} \times dl_j \\ \int_{\theta_j=0}^{\theta_j=2\pi} R_j \times \int_{\theta_k=0}^{\theta_k=2\pi} \frac{r_{j \leftarrow k w} \times dl_k}{\|r_{j \leftarrow k w}\|^3} \times dl_j \end{bmatrix}$$

where Fig. 2 provides an overview of this integration.

C. “Far-Field” Approximation Model

“Far-field” model [11] provides a computationally friendly approximated magnetic field. We assume the size of the

coil loop is much smaller than the relative distance, i.e., $|R_i| \ll |r_{j \leftarrow k}|$. Then, we get $1/|r| \approx 1/|s_{ij}| + s_{ij}R_i/|s_{ij}|^3$. This approximation derives dipole model of the multilayer coil as j th magnetic moment $\mu_j(t) \in \mathbb{R}^3$ [Am²] at time t

$$\mu_j(t) = \{\mathbf{b}\}^\top \mu_{j(t)}^b, \quad \mu_{j(t)}^b \triangleq N_t A [c_{jx(t)}; c_{jy(t)}; c_{jz(t)}] \quad (2)$$

where the current strength $c_{j(x,y,z)}(t)$ along with x, y, z -axis in j th body-fixed frame. Its magnetic field $B_k(\mu_k, r_{jk}) = \frac{\mu_0}{4\pi d_{jk}^3} (3M_k \mathbf{e}_r - \mu_k)$ where $M_k = \mu_k \mathbf{e}_r$, $d_{jk} = \|\mathbf{r}_{jk}\|$, and $\mathbf{e}_r = \mathbf{r}_{jk}/d_{jk}$. This also simplifies the magnetic field interaction model $\mathbf{f}_{j \leftarrow k} = \nabla(\mu_j B_k)$ and $\boldsymbol{\tau}_{j \leftarrow k} = \mu_j \times B_k$ where $\mathbf{f}_{j \leftarrow k} = \frac{3\mu_0}{4\pi d^4} ((\mu_k \mu_j - 5M_k M_j) \mathbf{e}_r + M_k \mu_j + M_j \mu_k)$.

III. COIL GEOMETRY INFORMATION AND DECENTRALIZED DIPOLE ALLOCATION

A. Three-Axis Coil Geometry Information with Coil Offset

We extend the interaction model in subsection II-B to a three-axis coil with offset illustrated in Fig. 2 to define the ‘‘coil geometry information vector.’’ We assume n agents have identical circular triaxial air-core coils whose radius is $a = a_j = a_k$, and the j th dipole moment $\mu_j(t) \in \mathbb{R}^3$ at time t in Eq. (2). We define the coil geometry vector of 3-axis agents between each axes $v, w = (x, y, z)$ as $\mathbf{g}_{jv \leftarrow kw} \in \mathbb{R}^6$ that includes the circulant integration term:

$$\begin{aligned} \mathbf{g}_{jv \leftarrow kw} (r_{j \leftarrow k}, C_j, a) &\triangleq \begin{bmatrix} \mathbf{g}_{jv \leftarrow kw}^{\text{pos}} (r_{j \leftarrow k}, C_j, a) \\ \mathbf{g}_{jv \leftarrow kw}^{\text{rot}} (r_{j \leftarrow k}, C_j, a) \end{bmatrix} \\ &\triangleq \begin{bmatrix} \int_{\theta_{jv}=0}^{\theta_{jv}=2\pi} \left(\mathbf{g}_{jv \leftarrow kw}^{\text{inner}}(\theta_{jv}) \right) \times d\mathbf{l}_{jv}(\theta_{jv}) \\ \int_{\theta_{jv}=0}^{\theta_{jv}=2\pi} R_{jv}(\theta_{jv}) \times \left(\mathbf{g}_{jv \leftarrow kw}^{\text{inner}}(\theta_{jv}) \right) \times d\mathbf{l}_{jv}(\theta_{jv}) \end{bmatrix} \end{aligned} \quad (3)$$

where the inner circular integration term $\mathbf{g}_{jv \leftarrow kw}^{\text{inner}} \in \mathbb{R}^3$ is

$$\mathbf{g}_{jv \leftarrow kw}^{\text{inner}}(\theta_{jv}) \triangleq \int_{\theta_{kw}=0}^{\theta_{kw}=2\pi} \frac{r_{jv \leftarrow kw}(\theta_{jv}, \theta_{kw}) \times d\mathbf{l}_{kw}(\theta_{kw})}{\|r_{jv \leftarrow kw}(\theta_{jv}, \theta_{kw})\|^3}$$

This defines the matrix $G_{j \leftarrow k} \in \mathbb{R}^{6 \times 9}$

$$\begin{cases} G_{j \leftarrow k} = A^{-2} [\mathbf{g}_{j \leftarrow k_x} & \mathbf{g}_{j \leftarrow k_y} & \mathbf{g}_{j \leftarrow k_z}] \\ \mathbf{g}_{j \leftarrow k_w} = [\mathbf{g}_{jx \leftarrow kw}^{\text{off}} & \mathbf{g}_{jy \leftarrow kw}^{\text{off}} & \mathbf{g}_{jz \leftarrow kw}^{\text{off}}] \\ \mathbf{g}_{jv \leftarrow kw}^{\text{off}} = \begin{bmatrix} I_3 & O_3 \\ [r_{jv}^{\text{off}}]_{\times} & I_3 \end{bmatrix} \mathbf{g}_{jv \leftarrow kw} \end{cases} \quad (4)$$

Finally, the j th input due to the magnetic field generated by the k th agent $u_{j \leftarrow k} = [f_{j \leftarrow k}; \tau_{j \leftarrow k}]$ and the total input on the j -agents $u_j = [f_j; \tau_j]$ due to the neighbor agents \mathcal{N}_j are

$$u_{j \leftarrow k} = \frac{\mu_0}{4\pi} G_{j \leftarrow k} (\mu_k^b \otimes \mu_j^b), \quad u_j = \sum_{k \in \mathcal{N}_j} u_{j \leftarrow k}. \quad (5)$$

B. Decentralized Dipole Allocation Using Alternating Current

We derive the control currents in a decentralized manner for simultaneous control of relative position and absolute attitude by extending the far-field study [15]. We first summarize alternating current (AC) modulation for multi-agent control.

Assumption 1. The j th agent apply periodic $\mu_j(t)$ for coils:

$$\mu_j(t) = s_j \sin \omega t + c_j \cos \omega t.$$

where ω [rad/s] is the angular frequency and sufficiently higher than the system dynamics time constant, i.e., $\frac{d\bar{x}}{dt} = \int_0^T \frac{dx}{d\tau}(t, \tau) \frac{d\tau}{T} + \epsilon$ and $\epsilon \ll 1$.

We calculate s_j and c_j so that the average value of the electromagnetic force $f_{j \leftarrow k}^{\text{avg}}$ and torque $\tau_{j \leftarrow k}^{\text{avg}}$ matches the control command values f_{jc}, τ_{jc} [12], [14], i.e.,

$$\sum_{k \in \mathcal{N}_j} \left[\int_T f_{j \leftarrow k}(u) \frac{du}{T} \right] \triangleq \sum_{k \in \mathcal{N}_j} \left[\int_T f_{j \leftarrow k}^{\text{avg}} \right] \equiv \begin{bmatrix} f_{jc} \\ \tau_{jc} \end{bmatrix}.$$

Based on Eq. (5), the averaged electromagnetic force and torque between two agents equipped with three-axis coils are

$$\begin{aligned} \begin{bmatrix} f_{j \leftarrow k}^{\text{avg}} \\ \tau_{j \leftarrow k}^{\text{avg}} \end{bmatrix} &\triangleq \int_T \frac{\mu_0}{4\pi} G_{j \leftarrow k} (\mu_k^b(u) \otimes \mu_j^b(u)) \frac{du}{T} \\ &\approx \frac{1}{2} \frac{\mu_0}{4\pi} G_{j \leftarrow k} (s_k^b \otimes s_j^b + c_k^b \otimes c_j^b) \end{aligned} \quad (6)$$

Then, the decentralized derivation of control currents that extends the far-field model one [15] is

$$\begin{cases} \begin{bmatrix} {}^a s_j \\ {}^a c_j \end{bmatrix} = \left(\frac{\mu_0}{8\pi} G_{j \leftarrow k}^a ({}^a s_k, {}^a c_k) \otimes E_3 \right)^{-1} \begin{bmatrix} {}^a f_{j \leftarrow k}^{\text{(avg)}} \\ {}^a \tau_{j \leftarrow k}^{\text{(avg)}} \end{bmatrix} \\ \begin{bmatrix} {}^a s_k \\ {}^a c_k \end{bmatrix} = \left(\frac{\mu_0}{8\pi} G_{j \leftarrow k}^a (E_3 \otimes [{}^a s_j, {}^a c_j]) \right)^{-1} \begin{bmatrix} {}^a f_{j \leftarrow k}^{\text{(avg)}} \\ {}^a \tau_{j \leftarrow k}^{\text{(avg)}} \end{bmatrix} \end{cases} \quad (7)$$

where we use $(\mathbf{a} \otimes \mathbf{b} + \mathbf{c} \otimes \mathbf{d}) = ([\mathbf{a}, \mathbf{c}] \otimes E_3) [\mathbf{b}; \mathbf{d}] = (E_3 \otimes [\mathbf{b}, \mathbf{d}]) [\mathbf{a}; \mathbf{c}]$ for arbitrary vectors $\mathbf{a}, \mathbf{b}, \mathbf{c}, \mathbf{d}$.

IV. LEARNING-BASED COIL GEOMETRY APPROXIMATION

This section designs an exact magnetic field approximation using a multilayer perceptron (MLP) model that captures coil-specific geometric features in Eq. (3) with its certification. The resulting pseudocode for offline training and online inference is presented in Algorithm 1.

A. Minimum-Dimensional Sample Collection and Learning

We first introduce the data collection strategy for consistent learning and reducing the sample space. For arbitrary j th and k th agents with the coil radius a_{NN} , we assume the coil geometry information $\mathbf{g}_{jv \leftarrow kw}^a$ in Eq. (3) is given:

$$\mathbf{g}_{jv \leftarrow kw}^a (r_{j \leftarrow k}^a, \sigma_j, \sigma_k, a_{\text{NN}}) \in \mathbb{R}^6$$

where arbitrary attitude parameter σ_j and σ_k is from the arbitrary reference frame \mathcal{A} to j th and k th body-fixed frame, respectively. We reduce sample region from 9-dimensional data $(r_{j \leftarrow k}^a, \sigma_j, \sigma_k)$ to 4-dimensional one $(\hat{r}_{j \leftarrow k}^{dkw}, \phi)$. The following two-coordinate transformation achieves this: 1) the k th reference coil lies within the x - y plane and 2) the j th coil lies within the x - z plane of the k th reference coil, as illustrated in Fig. 1. We first defines the unit vectors $\mathbf{n}_{k(x,y,z)}$ along with each axes of k th body-fixed frame $C^{A/Bk}(\sigma_k)$:

$$[\mathbf{n}_{kx}^a \quad \mathbf{n}_{ky}^a \quad \mathbf{n}_{kz}^a] \triangleq C^{A/Bk}(\sigma_k).$$

We define three coordinate frame B_{kx}, B_{ky}, B_{kz} such that each $\mathbf{n}_{k(x,y,z)}$ corresponds to its z -axis and its transformation matrixes $C^{A/Bk(x,y,z)} \in \mathbb{R}^{3 \times 3}$ for three axes is

$$C^{A/Bk(\mathbf{z}, \mathbf{x}, \mathbf{y})} \triangleq \begin{bmatrix} \mathbf{n}_{k(x,y,z)}^a & \mathbf{n}_{k(y,z,x)}^a & \mathbf{n}_{k(z,x,y)}^a \end{bmatrix} \quad (8)$$

where $C^{A/B_k}(\sigma_k) = C^{A/B_{k_z}}$ and this achieves that the k_w th reference coil lies within the x - y plane. We next adjust the direction of $r_{j \leftarrow k}$ to make its z -component positive by

$$\begin{bmatrix} r_{j \leftarrow k}^{b_{k_w}} \\ r_{j \leftarrow k}^{b_{k_w}} \\ r_{j \leftarrow k}^a \end{bmatrix} \triangleq \left(I_2 \otimes C^{B_{k_w}/A} \right) \begin{bmatrix} \text{sgn} \left(n_{k_w}^{a \top} r_{j \leftarrow k}^a \right) r_{j \leftarrow k}^a \\ n_{j \leftarrow k}^a \end{bmatrix} \quad (9)$$

where $\text{sgn}(\cdot)$ denotes the sign function and $\text{sgn}(0) \triangleq 1$. The following transformation achieves that the j th coil lies within the $x_+ - z_+$ plane of the k_w th reference coil:

$$C^{D_{j \leftarrow k_w}/A} = C^{D_{j \leftarrow k_w}/B_{k_w}} C^{B_{k_w}/A} \\ C^{D_{j \leftarrow k_w}/B_{k_w}} \triangleq \begin{bmatrix} C\theta_{b_{k_w}} & S\theta_{b_{k_w}} & 0 \\ -S\theta_{b_{k_w}} & C\theta_{b_{k_w}} & 0 \\ 0 & 0 & 1 \end{bmatrix} \quad (10)$$

where $\theta_{b_{k_w}} \triangleq \tan^{-1} \left(r_{j \leftarrow k(2)}^{b_{k_w}}, r_{j \leftarrow k(1)}^{b_{k_w}} \right)$. Since this imposes $r_{j \leftarrow k(2)}^{d_{k_w}} = 0$, we reduce the input into two dimensional vector $\hat{r}_{j \leftarrow k}^{d_{k_w}}$. Moreover, the three-dimensional information of $n_{j_v}^{d_{k_w}} = [c_{\phi(1)} s_{\phi(2)}; s_{\phi(1)} s_{\phi(2)}; c_{\phi(2)}]$ is reduced into $\phi \in \mathbb{R}^2$ by the spherical coordinate representation using azimuth $\phi(1) \in (-\pi, \pi]$ and elevation $\phi(2) \in (0, \pi)$. As a result, we obtain the reduced-dimensional input vector:

$$\hat{r}_{j \leftarrow k}^{d_{k_w}} \triangleq \begin{bmatrix} r_{j \leftarrow k(1)}^{d_{k_w}} \\ r_{j \leftarrow k(3)}^{d_{k_w}} \end{bmatrix}, \quad \phi \triangleq \begin{bmatrix} \tan^{-1} \left(n_{j_v(2)}^{d_{k_w}}, n_{j_v(1)}^{d_{k_w}} \right) \\ \cos^{-1} \left(n_{j_v(3)}^{d_{k_w}} \right) \end{bmatrix} \quad (11)$$

To compensate the sign change of input data in Eq. (9), the label data is also modified as follows:

$$g_{j_v \leftarrow k_w}^{d_{k_w}} \triangleq \left(\begin{bmatrix} \text{sgn} \left(n_{k_w}^{a \top} r_{j \leftarrow k}^a \right) & 0 \\ 0 & 1 \end{bmatrix} \otimes C^{D_{j \leftarrow k_w}/A} \right) g_{j_v \leftarrow k_w}^a \quad (12)$$

These derives input $(\hat{r}_{j \leftarrow k}^{d_{k_w}}, \phi)$ and label $g_{j_v \leftarrow k_w}^{d_{k_w}}$ and we stack N_s data $X = [\mathbf{r}, \phi] \in \mathbb{R}^{N_s \times 4}$ and $Y \in \mathbb{R}^{N_s \times 6}$

$$\mathbf{r} = \begin{bmatrix} \hat{r}_{j \leftarrow k}^{d_{k_w}(1)\top} \\ \vdots \\ \hat{r}_{j \leftarrow k}^{d_{k_w}(N_s)\top} \end{bmatrix}, \quad \phi = \begin{bmatrix} \phi(1)\top \\ \vdots \\ \phi(N_s)\top \end{bmatrix}, \quad \mathbf{Y} = \begin{bmatrix} g_{j_z \leftarrow k_z}^{d_{k_w}(1)\top} \\ \vdots \\ g_{j_z \leftarrow k_z}^{d_{k_w}(N_s)\top} \end{bmatrix}$$

We train our MLP \mathbf{g} to minimize an arbitrary loss function $f(\cdot)$: $\theta_w^*, \theta_b^* = \text{argmin} \sum_{j=1}^{N_s} f(\|\mathbf{Y}^{(j)\top} - \hat{\mathbf{Y}}^{(j)\top}\|)$ where $\hat{\mathbf{Y}}^{(j)}$ is estimated values by \mathbf{g} using training data set $\mathcal{T}_{a_{\text{NN}}} = \{(X^{(i)}, Y^{(i)})\}_{i=1}^{N_s}$ in given compact set $\mathcal{S}_{a_{\text{NN}}}$ with $2a_{\text{NN}} < r$:

$$\mathcal{S}_{a_{\text{NN}}} = \left\{ \begin{array}{l} r_{j \leftarrow k} \in \mathbb{R}^2 \\ \phi \in \mathbb{R}^2 \end{array} \left| \begin{array}{l} r \leq \|r_{j \leftarrow k}\| \leq \bar{r}, \\ \phi(1) \in [-\pi, \pi] \\ \phi(2) \in [0, \pi] \end{array} \right. \right\}$$

Here, we obtain $\hat{\mathbf{Y}}^{(j)} = W_{dl} \times \mathbf{g}(W_{di}^{-1}(X^{(j)} - b_{di}), \theta) + b_{dl}$ by \mathbf{g} using preprocessing matrices $W_{dl, di}$ and vectors $b_{dl, di}$, e.g., normalization or standardization.

B. Generalization for Arbitrary Radius Coil Inference

We can apply the learned model \mathbf{g} for coil radius a_{NN} to different coils with coil radius $a_{\text{inf}} \triangleq \gamma a_{\text{NN}}$ via appropriate transformations without retraining.

Theorem IV.1. For given MLP model $\mathbf{g}(X, \theta) = \mathbf{g}([\mathbf{r}, \phi], \theta)$ learned coil geometry information for coil radius a_{NN} in $\mathcal{S}_{a_{\text{NN}}}$,

consider the coil radius $a_{\text{inf}} \triangleq \gamma a_{\text{NN}}$ and the new data in sample region $\mathcal{S}_{a_{\text{inf}}}$ that bounded by constants of $\mathcal{S}_{a_{\text{NN}}}$:

$$\mathcal{S}_{a_{\text{inf}}} = \left\{ \begin{array}{l} r_{j \leftarrow k} \in \mathbb{R}^2 \\ \phi \in \mathbb{R}^2 \end{array} \left| \begin{array}{l} r \leq \frac{\|r_{j \leftarrow k}\|}{\gamma} \leq \bar{r}, \\ \phi(1) \in [-\pi, \pi] \\ \phi(2) \in [0, \pi] \end{array} \right. \right\}.$$

Then, \mathbf{g} derives $g_{j_v \leftarrow k_w}^a(r_{j \leftarrow k}^a, \sigma_j, \sigma_k, a_{\text{inf}})$ as

$$g_{j_v \leftarrow k_w}^a(r_{j \leftarrow k}^a, \sigma_j, \sigma_k, a_{\text{inf}}) = \begin{bmatrix} I_3 & O \\ O & \gamma I_3 \end{bmatrix} \mathbf{g} \left(\begin{bmatrix} r^{(i)} \\ \gamma \\ \phi^{(i)} \end{bmatrix}, \theta \right) \quad (13)$$

Proof. By substituting r/γ and ϕ into the definition of $g_{j_v \leftarrow k_w}^a$ in Eq. (3), we obtain Eq. (13). \square

C. Certified Error Bounds of Coil Geometry Information

Finally, we derive the theoretical upper bound on the learning error. Followed by Eq. (1), we obtain the error bound $\sup_{x \in \mathcal{S}_{a_{\text{NN}}}} [\|\mathbf{g}_{(x)}^{\text{pos}} - \hat{\mathbf{g}}_{(x)}^{\text{pos}}\|; \|\mathbf{g}_{(x)}^{\text{rot}} - \hat{\mathbf{g}}_{(x)}^{\text{rot}}\|] - \sup_{x' \in \mathcal{T}_{a_{\text{NN}}}} [\|\mathbf{g}_{(x')}^{\text{pos}} - \hat{\mathbf{g}}_{(x')}^{\text{pos}}\|; \|\mathbf{g}_{(x')}^{\text{rot}} - \hat{\mathbf{g}}_{(x')}^{\text{rot}}\|] \leq [\delta g^{\text{pos}}; \delta g^{\text{rot}}] \triangleq (L_g + L_{\mathbf{g}}) [\rho_{\mathcal{S}(a_{\text{NN}}, r)}; \rho_{\mathcal{S}(a_{\text{NN}}, \phi)}]$ where a constant Lipchitz matrix of true function $L_g \in \mathbb{R}^{2 \times 2}$ and MLP $L_{\mathbf{g}} \in \mathbb{R}^{2 \times 2}$, respectively, $\rho_{\mathcal{S}(a_{\text{NN}}, r)}$ and $\rho_{\mathcal{S}(a_{\text{NN}}, \phi)}$ are covering radius about position and attitude. We can derives $L_{\mathbf{g}}$ as $L_{\mathbf{g}} \lesssim \sigma(W_{dl}) (\|\phi\|_{\text{Lip}}^L \prod_{l=1}^{L+1} \sigma(W^{(l)}) \sigma(W_{di}^{-1})) \leq \sigma(L_g)$ or $L_{\mathbf{g}} \triangleq [L_{\mathbf{g}_{\text{pos}}}^{\text{pos}}, L_{\mathbf{g}_{\text{pos}}}^{\text{rot}}; L_{\mathbf{g}_{\text{rot}}}^{\text{pos}}, L_{\mathbf{g}_{\text{rot}}}^{\text{rot}}]$ where $L_{\mathbf{g}_{\text{pos, rot}}}^{\text{pos, rot}}$ with $L_{\mathbf{g}0} = \|\phi\|_{\text{Lip}}^L \prod_{l=2}^L \sigma(W^{(l)})$ are

$$\begin{cases} L_{\mathbf{g}_{\text{pos}}}^{\text{pos}} = L_{\mathbf{g}0} \times \sigma \left(W_{dl(1:3,:)} W^{(L+1)} \right) \times \sigma \left(W^{(1)} W_{di(1:1:2)}^{-1} \right) \\ L_{\mathbf{g}_{\text{pos}}}^{\text{rot}} = L_{\mathbf{g}0} \times \sigma \left(W_{dl(1:3,:)} W^{(L+1)} \right) \times \sigma \left(W^{(1)} W_{di(1:3:4)}^{-1} \right) \\ L_{\mathbf{g}_{\text{rot}}}^{\text{pos}} = L_{\mathbf{g}0} \times \sigma \left(W_{dl(4:6,:)} W^{(L+1)} \right) \times \sigma \left(W^{(1)} W_{di(1:1:2)}^{-1} \right) \\ L_{\mathbf{g}_{\text{rot}}}^{\text{rot}} = L_{\mathbf{g}0} \times \sigma \left(W_{dl(4:6,:)} W^{(L+1)} \right) \times \sigma \left(W^{(1)} W_{di(1:3:4)}^{-1} \right) \end{cases}$$

The following theorem derives a constant Lipchitz matrix of true function $L_g \in \mathbb{R}^{2 \times 2}$ as $L_g = [L_{\mathbf{g}_{\text{pos}}}^{\text{pos}}, L_{\mathbf{g}_{\text{pos}}}^{\text{rot}}; L_{\mathbf{g}_{\text{rot}}}^{\text{pos}}, L_{\mathbf{g}_{\text{rot}}}^{\text{rot}}]$ and the upper bound of $\Delta_g(x) \triangleq [\|\mathbf{g}_{(x)}^{\text{pos}} - \hat{\mathbf{g}}_{(x)}^{\text{pos}}\|; \|\mathbf{g}_{(x)}^{\text{rot}} - \hat{\mathbf{g}}_{(x)}^{\text{rot}}\|]$.

Theorem IV.2 (Certified Error Bounds). Consider N optimally placed training data set $\mathcal{T}_{a_{\text{NN}}}$ in $\mathcal{S}_{a_{\text{NN}}}$. Then, the prediction error for a coil radius a_{NN} is bounded as $\sup_{x \in \mathcal{S}_{a_{\text{NN}}}} \Delta_g(x) \leq \sup_{x' \in \mathcal{T}_{a_{\text{NN}}}} \Delta_g(x') + [\delta g^{\text{pos}}; \delta g^{\text{rot}}]$:

$$\begin{bmatrix} \delta g^{\text{pos}} \\ \delta g^{\text{rot}} \end{bmatrix} = (L_g + L_{\mathbf{g}}) \begin{bmatrix} \rho_{\mathcal{S}(a_{\text{NN}}, r)} \\ \rho_{\mathcal{S}(a_{\text{NN}}, \phi)} \end{bmatrix} \\ = \left(L_0 \begin{bmatrix} 1 & a_{\text{NN}} + r_{\text{min}}/2 \\ a_{\text{NN}} & a_{\text{NN}}(a_{\text{NN}} + r_{\text{min}}) \end{bmatrix} + L_{\mathbf{g}} \right) \begin{bmatrix} \sqrt{r^2 - r^2} \\ \frac{\sqrt{2\pi}}{2N^{1/4}} \\ \frac{\sqrt{2\pi}}{N^{1/4}} \end{bmatrix} \quad (14)$$

where $L_0 = 2(2\pi a_{\text{NN}})^2 / r_{\text{min}}^3$, $r_{\text{min}} \leq \inf_{\theta_j, \theta_{k_w}} \|r_{j_v \leftarrow k_w}\|$.

Proof. See Appendix A. \square

Along with the transformation for the coil radius $a_{\text{inf}} = \gamma a_{\text{NN}}$ in Theorem IV.1, the prediction error for a coil radius a_{inf} is bounded as $\sup_{x \in \mathcal{S}_{a_{\text{inf}}}} \Delta_g(x) = [I_3, O; O, \gamma I_3] \sup_{x \in \mathcal{S}_{a_{\text{NN}}}} \Delta_g(x)$.

V. VALIDATION BY SATELLITE DOCKING APPLICATION

We validate the proposed learning-based current calculation for docking control of the target and chaser satellite. We

Algorithm 1 Coil geometry learning in reference frame (A)

1: — **Offline Phase** —
2: **Inputs:** sample number n_s
3: **Outputs:** MLP weights θ_w^* , MLP bias θ_b^*
4: **for** $i \in [1, \dots, n_s]$ **do**
5: Generate random $r_{j \leftarrow k}^{a(i)}$ and $n_{j,k}^{a(i)}$
6: Derive $C^{A/B_{kz}} = [{}^a n_{k_x} \quad {}^a n_{k_y} \quad {}^a n_{k_z}]$ in Eq. (8)
7: Derive $C^{D_{j \leftarrow kz}/B_{kz}}$ in Eq. (10) and $r_{j \leftarrow k}^{d_{j \leftarrow kz}}$
8: Stack inputs $\mathbf{X}^{(i)} = [r_{j \leftarrow k}^{d_{j \leftarrow kz}(i)}, n_{j_z}^{d_{j \leftarrow kz}(i)}]^\top$
9: Calculate labels $\mathbf{Y}^{(i)} = g_{j_v \leftarrow k_w}^{d_{j_v \leftarrow k_w}}$ in Eq. (12)
10: **end for**
11: Derive θ_w^*, θ_b^* by \mathbf{X} and \mathbf{Y} , e.g., Eq. (15)
12: — **Online Phase** —
13: **Inputs:** 1) ${}^a r_{j \leftarrow k}$, 2) ${}^a n_{j,k(x,y,z)}$, 3) θ_w^*, θ_b^* , 4) the area enclosed by the coil A
14: **Outputs:** Exact model coefficient matrix ${}^a Q_{j \leftarrow k} \in \mathbb{R}^{6 \times 9}$
15: **for** $k_w \in [k_x, k_y, k_z]$ **do**
16: Derive $C^{D_{j \leftarrow k_w}/A}$ in Eq. (10) and $r_{j \leftarrow k}^{d_{j \leftarrow k_w}}$
17: **for** $j_v \in [j_x, j_y, j_z]$ **do**
18: Derive $n_{j_v}^{d_{j \leftarrow k_w}}$ and stack $x = [r_{j \leftarrow k}^{d_{j \leftarrow k_w} \top}, n_{j_v}^{d_{j \leftarrow k_w} \top}]$
19: Infer $g_{j_v \leftarrow k_w}^{d_{j \leftarrow k_w}} = \mathbf{g}(x, \theta)$ in Eq. (12)
20: Calculate $g_{j_v \leftarrow k_w}^a = (I_2 \otimes C^{A/D_{j \leftarrow k_w}}) g_{j_v \leftarrow k_w}^{d_{j \leftarrow k_w}}$
21: Calculate $g_{j_v \leftarrow k_w}^{\text{off}} = \begin{bmatrix} I_3 & O_3 \\ [r_{j_v, \text{off}}]_\times & I_3 \end{bmatrix} g_{j_v \leftarrow k_w}^a$
22: **end for**
23: Stack $[g_{j \leftarrow k_w}] = [g_{j_x \leftarrow k_w, \text{off}} \quad g_{j_y \leftarrow k_w, \text{off}} \quad g_{j_z \leftarrow k_w, \text{off}}]$
24: **end for**
25: Stack $G_{j \leftarrow k} = A^{-2} \begin{bmatrix} [g_{j \leftarrow k_x}] & [g_{j \leftarrow k_y}] & [g_{j \leftarrow k_z}] \end{bmatrix}$

TABLE I: Sample region information and covering radii.

	$\frac{r/\bar{r}}{2a_{\text{NN}}} \text{ [m]}$	N [-]	$\rho_{\mathcal{S}(a_{\text{NN}}, r)} / \rho_{\mathcal{S}(a_{\text{NN}}, \phi)}$
$\mathcal{S}_{a_{\text{NN}}}^A$	1.0005 / 1.075	1.0e ⁹	0.66e ⁻³ / 14.10e ³
$\mathcal{S}_{a_{\text{NN}}}^B$	1.4 / 1.9	2e ⁸	3.24e ⁻³ / 21.08e ³
$\mathcal{S}_{a_{\text{NN}}}^C$	1.046 / 4.0	2.5e ⁷	16.38e ⁻³ / 35.45e ³

primarily compare docking results obtained by the learned exact model and the far-field approximation model in subsection II-C. We first train our model \mathbf{g} by coil radius $a_{\text{NN}} = 0.3$ in subsection V-A and apply it to numerical simulation for $a_{\text{inf}} = 0.15$ in subsection V-B and experimental test $a_{\text{inf}} = 0.075$ in subsection V-C to show its universality.

A. Offline Training of Coil Geometry Model

We first train the magnetic interaction model \mathbf{g} by coil radius $a_{\text{NN}} = 0.3$ based on our framework. This study collects 11 million samples in three domains $\mathcal{S}_{a_{\text{NN}}}^A, \mathcal{S}_{a_{\text{NN}}}^B, \mathcal{S}_{a_{\text{NN}}}^C$ as shown in Table V-A. We use a model with two hidden layers, each with 256 and 128 neurons, respectively, that use Layer Normalization and GELU activation whose Lipschitz constant is bounded $\|\phi\|_{\text{Lip}} \leq 1.129$. We train by the Adam optimizer [18], a batch size of 131,072 for pre-training and 1,024 for fine-tuning, and the smooth L1 loss function $f(\cdot)$, with a

spectral normalization regularization term [19]:

$$\mathcal{L}(\theta_w, \theta_b) = \sum_{j=1}^{N_s} \sum_{i=1}^6 \frac{\rho_\delta(Y_i^{(j)} - \hat{Y}_i^{(j)})}{6N_s} + \lambda_{\text{sn}} \sum_{l=1}^{L+1} \left[\max(0, \sigma_{\max}(W^{(l)}) - \bar{w}) \right]^2 \quad (15)$$

where Huber loss function $\rho_\delta(r_i) = r_i^2/2$ if $|r_i| < \delta$ and otherwise, $\delta(|r_i| - 1/2)$, and \bar{w} is the user-defined constant. An implementation that enforces the Lipschitz constant exactly, rather than using a penalty, is described in [17], [19]. The learning rate is scheduled using cosine annealing from $1e^{-2}$ to $1e^{-6}$ for pre-training and $1e^{-6}$ to $1e^{-16}$ for fine-tuning.

The training process for $\lambda_{\text{sn}} = 0$ converged with a test loss of $4.11e^{-3}$, a training loss of $3.01e^{-3}$, and $\bar{\sigma}(L_g) = 1.17e^7$. Since the Lipschitz constant of a true function is calculated as $\bar{\sigma}(L_g) = 40.47$ in $\mathcal{S}_{a_{\text{NN}}}^A$, this $\bar{\sigma}(L_g)$ is significantly larger than true one. This motivates us to add spectral normalization term and the training process for $\lambda_{\text{sn}} = 1e^{-3}$ converged with a test loss of $5.29e^{-3}$, a training loss of $5.34e^{-3}$, and $\bar{\sigma}(L_g^{\text{SN}}) = 44.79$. This agreement between the two losses indicates acceptable generalization performance.

B. Numerical Validation for Spacecraft Docking

We first demonstrate the effectiveness of the learned exact model through numerical docking simulations, and Table II summarizes the simulation conditions. To achieve the target position and attitude, we design PD controllers and update the reference states using third-order splines at 0.1-second intervals to satisfy the current upper limit. Note that numerical integration uses the exact model in Eq. (5) and confirms angular momentum conservation, affirming the validity of our simulation. For the dipole allocation to achieve controller input, we assume the following.

Assumption 2. Only the 1st (target) satellite has RWs to control its attitude in Appendix B, and the attitude of the 2nd (chaser) satellite is controlled by the electromagnetic torque.

Assumption 3. The current amplitudes on the 1st (target) satellite are predetermined in Eq. (16) with $c_{\text{amp}0} = 3A$ to ensure regularity of inverse matrix in Eq. (7):

$$s_1^{b_1} = \begin{bmatrix} c_{\text{amp}0} \frac{\|r_{12}(t)\|}{\|r_{12}(0)\|} [0.1 \quad 0.3 \quad 0.7]^\top \\ c_{\text{amp}0} \frac{\|r_{12}(t)\|}{\|r_{12}(0)\|} - s_1^{b_1} \end{bmatrix} \in \mathbb{R}^3 \quad (16)$$

We compare the docking results using the exact model and the far-field approximation model. Figure 3 shows the time evolution of the relative states and electromagnetic control inputs. For the far-field model, we observe significant input errors around 200-250 seconds, and this leads to a collision as shown in Fig. 3e. Conversely, Fig. 3f shows that the exact model accomplishes the docking control for randomly generated 30 initial states. It is also worth noting that the 2nd satellite achieves attitude control solely through electromagnetic torque, which reaffirms the effectiveness of electromagnetic torque for attitude control [12], [14].

Next, we apply our trained magnetic interaction model \mathbf{g} to the docking control, and the results in Fig. 4a show successful

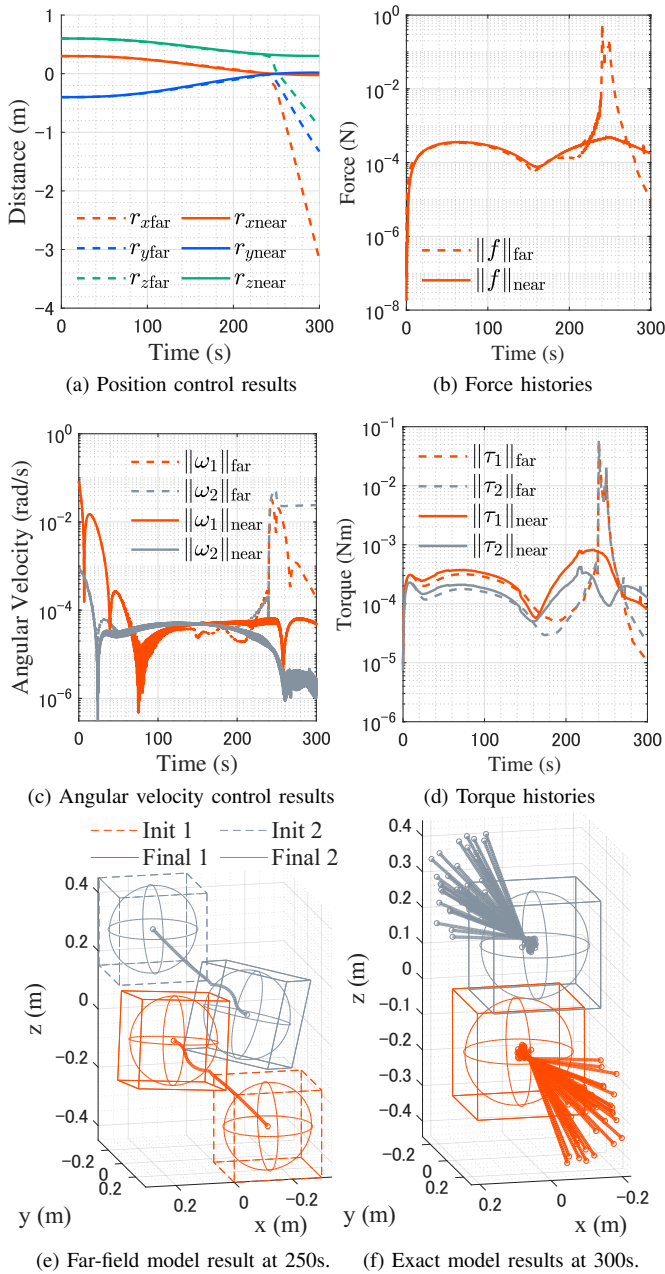


Fig. 3: Numerical results of two-satellite docking control using the far-field magnetic field approximation in Appendix II-C (Dashed lines) and the exact magnetic field model in Eq. (5) (solid lines). The target and chaser satellite are depicted in gray and red, respectively. The exact model results are based on 30 random initial conditions.

results for the newly generated 30 random initial states. On our PC, the average calculation time and its standard deviation decreased to approximately 1/1000 and 1/2500, respectively, indicating more consistent and stable computation. As the distance decreases, the Biot-Savart model increases the number of integration steps to ensure accuracy, whereas the MLP maintains a uniform computation regardless of the distance.

C. Experimental Validation for Docking Control

We validate our trained magnetic interaction model \mathbf{g} through a ground testbed for a docking situation. We briefly summarize the experimental setup; please see the detailed

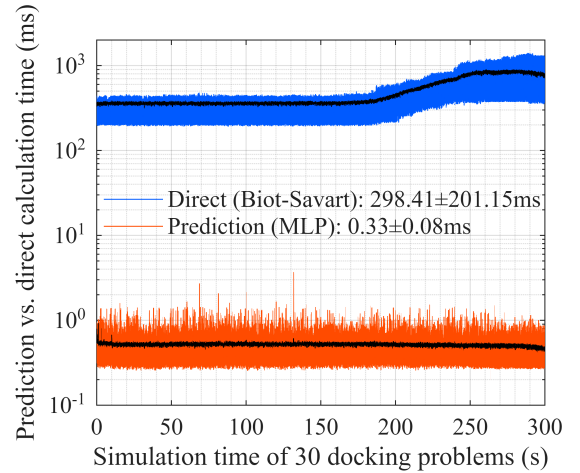
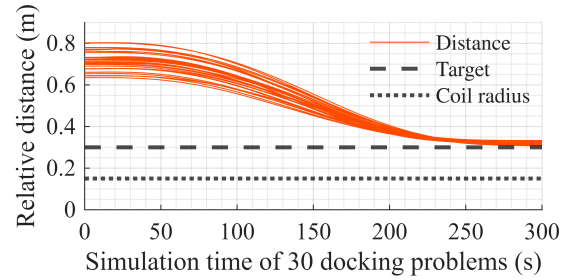


Fig. 4: The learned model-based docking control result. The time evolution of the distance and time comparison of direct computation (Biot-Savart double integral) and prediction using our model.

description in [13]. The testbed MTQ has two-axis coils to generate a magnetic field in the horizontal plane, and the second coil uses an iron core. As shown in Fig 5a, two MTQ mounts are on a linear air track and a single-axis air bearing, respectively. We measure relative position using a ToF sensor and absolute attitude using an AR marker-based camera pose estimation. The Pulse Per Second signal from GPS enables time synchronization for AC magnetic control with an accuracy of 0.1ms. Along with the assumption 2, we assume the MTQ on a linear track has RWs to fix its attitude, and only the attitude of the MTQ on air-bearing is controlled.

To compensate for the microgravity caused by linear track distortions, we design a PID controller for position and attitude control, updating its command values every 187.5 ms. Figures 5b and 5c show the initial and target conditions on the linear air track and single-axis air bearing in Fig. 5a. We calculate control current to realize the controller command value using the far-field model “dipole” and the learned model “cgl” trained in subsection V-A. We also conduct the experiment on the learned model \mathbf{g} with spectral normalization “cgl SN” and without it “cgl”. For every dipole allocation phase, the current amplitudes are calculated by the decentralized current allocation on Eq. (7). Unlike the assumption 3, we normalize the norm of sine and cosine amplitudes of two coils to satisfy the current limitation of the testbed.

Figures 5d and 5e show the experimental results of rel-

ative position and absolute attitude. Although their control commands are the same, far-field model-based control cannot stabilize the states at the target in some cases; otherwise, it increases steady-position errors. The reason is illustrated in Figs 5f and 5f that show the estimation results of coil geometry information vectors through each model with the constant $k \approx 2.205e^{-7}$. The black line indicates the ground truth of coil geometry information vectors between each axis, and the blue line indicates the error between truth and the dipole approximation model prediction. As the distance decreases, the approximation becomes invalid and can result in large errors accompanied by sign reversals, which is consistent with the numerical results presented in subsection V-B. In contrast, the learning-based model “cgl SN” accurately predicts the ground-truth data, and the red curve represents the error between truth and the learned model prediction. The theoretical upper bound of “cgl SN” derived in Theorem IV.2 estimates the prediction error bound correctly. As a result, the learning-based magnetic field control successfully achieves rapid state convergence for proximity operation. Comparing “cgl SN” and “cgl”, “cgl SN” achieves comparable—or even more stable—performance even though “cgl SN” exhibits relatively larger training errors as described in subsection V-A.

VI. CONCLUSIONS

This paper proposes a learning-based magnetic interaction modeling approach, along with its validation, that mimics the exact model. Our approximation model reduces the computational burden of the exact magnetic model while minimizing the far-field approximation error in proximity. We first extend a previous decentralized current calculation, which does not require inter-agent communication, to account for the precise model and coil offset. Then, we demonstrate that the traditional approximation loses accuracy in proximity, leading to unstable motion, such as collisions. In contrast, our learning-based magnetic field model simultaneously controls relative distance and attitude with a low computational load and high stability. Its applications include several sectors that require exceptional accuracy and responsiveness. Especially, fuel-free docking is a key technology for in-space assembly, station resupply, sample-return, and large-scale swarm formation.

APPENDIX

A. Proof: Theorem IV.2 (Certified Error Bounds)

Proof. We first derive blockwise Lipschitz constants $L_{g_{\text{pos,rot}}}^{\text{pos,rot}}$ of true function. We define the vectors $g_{\text{pos,rot}} \in \mathbb{R}^3$ associated with the kernel of the double integral in Eq. (3):

$$\begin{cases} g_{\text{pos}} = K_{(r,dl_k)} \times dl_j \\ g_{\text{rot}} = [R_j \times K_{(r,dl_k)}] \times dl_j \end{cases}, \quad K_{(r,dl_k)} = \frac{f_{(r)} \times dl_k}{\|f_{(r)}\|^3} \in \mathbb{R}^3$$

where arbitrary vector $f_{(r)} = r + C^{k/j}R_j - R_k$ with $\|f_{(r)}\| \geq r_{\min}$ and $R_j = a_{\text{NN}}[\cos \varphi_j, \sin \varphi_j, 0]^T$ where $r \in \mathbb{R}^3$. Here, the Jacobian of K satisfies $\|\partial K/\partial r\|_2 \leq \|I - 3\hat{f}_{(r)}\hat{f}_{(r)}^T\| \|dl_k\| / \|f_{(r)}\|^3 \leq 2\|dl_k\|/r_{\min}^3$ where we use $\hat{r} = r/\|r\|$, $\|dl_k\| \times \|dl_k\| = \|dl_k\|^2$, and $\lambda(I - 3\hat{f}_r\hat{f}_r^T) =$

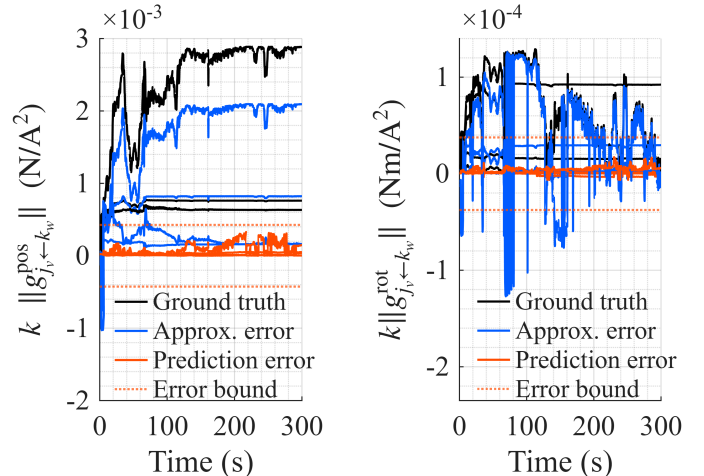
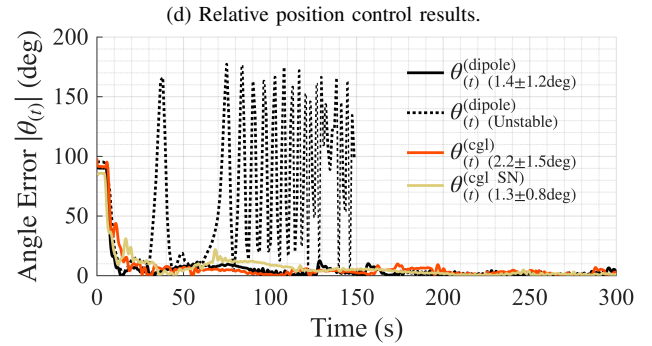
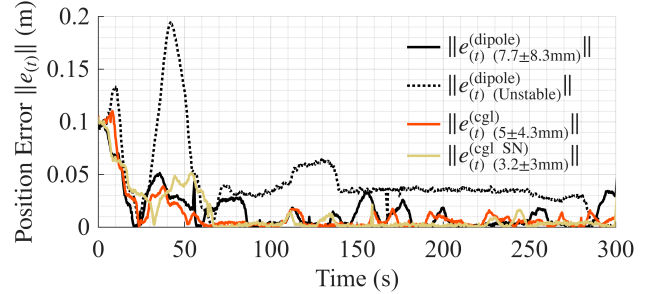
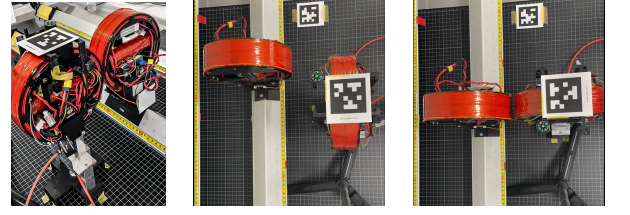


Fig. 5: Experimental results of two-satellite docking control using the learned magnetic interaction model on a microgravity testbed. With the constant $k = \gamma_{\mu/c}^2 \mu_0 / (8\pi A^2) \approx 2.205e^{-7}$ [H/m] applied, the y-axis values in Figs 5f and 5f indicate the coefficients relating the product of the two coil currents to the resulting force and torque. $\gamma_{\mu/c}$ [m²] is the design ratio of experimental coils between the maximum dipole and maximum current ($\gamma_{\mu/c} \approx 2.1$ [13]).

$\{1, 1, -2\}$. Applying $\hat{f} \|dl_k\| = \hat{f} \|dl_k\| = 2\pi a_{\text{NN}}$ yields the block-wise Lipschitz constants of g^{pos} as

$$L_{g_{\text{pos}}}^{\text{pos}} \leq L_0, \quad L_{g_{\text{rot}}}^{\text{pos}} \leq a_{\text{NN}}L_0, \quad L_0 = 2(2\pi a_{\text{NN}})^2 / r_{\min}^3$$

where $\|K\| \leq \|dl_k\| / \|f_{(r)}\|^2 \leq \|dl_k\| / r_{\min}^2$ and $\|\partial dl_j / \partial n_j\| \leq \|dl_j\|$. We next derive blockwise attitude

TABLE II: The numerical simulation setups in subsection V-B.

Parameters	Values	Parameters	Values
Coil radius	0.15 m	Coil turns	100
Satellite mass	20 kg	Altitude	700 km
AC amplitude limit	± 10 A	AC frequency	8π rad/s

Parameters	Values
Initial relative position and velocity	$[0.3; -0.4; 0.6]\text{m}, [0; 0; 0]\text{m/s}$
Initial quaternion	$[0; 0; 0; 1]$
Initial angular velocity (S/C 1)	$[0.01; 0.02; 0.08]\text{rad/s}$
Initial angular velocity (S/C 2)	$[1e^{-4}; 2e^{-4}; 8e^{-4}]\text{rad/s}$
Target relative position	$[0; 0; 0.3]\text{m}$
Target quaternion and angular velocity	$[0; 0; 0; 1], [0; 0; 0]\text{rad/s}$

Lipschitz constants. Let δn_j be denoted as the infinitesimal variation of the coil unit direction n_j in subsection IV-A. Then, the first-order variations with respect to n_j are $\|\delta g_{\text{pos}}\| = \left\| \left[\left(\frac{\partial K}{\partial f(r)} \frac{\partial f(r)}{\partial n_j} \delta n_j \right) \times dl_j + K \times \frac{\partial dl_j}{\partial n_j} \delta n_j \right] \right\| \leq \left(\frac{2a_{\text{NN}}}{r_{\text{min}}^3} + \frac{1}{r_{\text{min}}^2} \right) \|dl_j\| \|\delta n_j\|$ and $\|\delta g_{\text{rot}}\| = \left\| \left(\frac{\partial R_j}{\partial n_j} \delta n_j \times K + R_j \times \frac{\partial K}{\partial f(r)} \frac{\partial f(r)}{\partial n_j} \delta n_j \right) \times dl_j + (R_j \times K) \times \frac{\partial dl_j}{\partial n_j} \delta n_j \right\| \leq \left(\frac{2a_{\text{NN}}}{r_{\text{min}}^2} + \frac{2a_{\text{NN}}}{r_{\text{min}}^3} \right) \|dl_j\| \|\delta n_j\|$ where $\|\partial K / \partial f(r)\| \leq 2\|dl_k\|/r_{\text{min}}^3$, $\|R_j\| \leq a_{\text{NN}}$, $\|\partial f(r) / \partial n_j\| \leq a_{\text{NN}}$, $\|\partial R_j / \partial n_j\| \leq a_{\text{NN}}$, and $\|\partial K / \partial dl_k\| \leq \|r\|^{-2}$. Since the Jacobian $\partial n / \partial \phi \in \mathbb{R}^{3 \times 2}$ satisfies $\|(\partial n / \partial \phi)^\top \partial n / \partial \phi\|_2 = \|\text{diag}(\sin^2 \phi_{(2)}, 1)\|_2 = 1$, we obtain $\|\delta n_j\| \leq \|\delta \phi_j\|$. Integrating $\|dl_{j,k}\|$ over $\theta_{j,k}$ yields blockwise Lipschitz constants with respect to ϕ as

$$L_{g_{\text{pos}}}^{\text{rot}} \leq (a_{\text{NN}} + r_{\text{min}}/2) L_0, \quad L_{g_{\text{rot}}}^{\text{rot}} \leq (a_{\text{NN}} + r_{\text{min}}) a_{\text{NN}} L_0.$$

We mention the upper bound of $\rho_{\mathcal{S}_{\{(a_{\text{NN}}, r), (a_{\text{NN}}, \phi)\}}}$. Since N optimally placed points for the entire region, each point covers $\text{Vol}(\mathcal{S}_{\{(a_{\text{NN}}, r), (a_{\text{NN}}, \phi)\}}) / \sqrt{N}$. Moreover, n -dimensional ball of radius r generally has volume $r^n \pi^{n/2} / \Gamma(1 + n/2)$ where $\Gamma(\cdot)$ denotes the gamma function. These derive the deterministic upper bound as $\rho_{\mathcal{S}_{\{(a_{\text{NN}}, r), (a_{\text{NN}}, \phi)\}}} \leq \frac{\text{Vol}(\mathcal{S}_{\{(a_{\text{NN}}, r), (a_{\text{NN}}, \phi)\}})}{\sqrt{N} \pi^{n/2} / \Gamma(\frac{n}{2} + 1)}^{1/n}$ where $\rho_{\mathcal{S}} \leq (\text{Vol}(\mathcal{S}) / (\pi \sqrt{N}))^{1/2}$ for $n = 2$, $\text{Vol}(\mathcal{S}_{(a_{\text{NN}}, r)}) = (\pi/4)(\bar{r}^2 - r^2)$ and $\text{Vol}(\mathcal{S}_{(a_{\text{NN}}, \phi)}) = \pi(2\pi)$. These results concludes Eq. (14). \square

B. Earth Orbital and Attitude Motion Simulation

The relative motion in a circular orbit and the attitude dynamics of two satellites with a reaction wheel (RW) [12] is

$$\ddot{x} + 2\omega_o \dot{y} - 3\omega_o^2 x = u_x, \quad \ddot{y} - 2\omega_o \dot{x} = u_y, \quad \ddot{z} + \omega_o^2 z = u_z$$

$$J\dot{\omega} + \omega \times (J\omega + h_{\text{RW}}) = -\tau_{\text{RW}}, \quad \dot{h}_{\text{RW}} = \tau_{\text{RW}}$$

where $u_{x,y,z} \in \mathbb{R}$ is acceleration per unit mass along each axis, $\omega_o \approx 1.1e^{-3} \in \mathbb{R}$ denotes the orbital frequency, $J \in \mathbb{R}^{3 \times 3}$ is the moment of inertia, $\omega \in \mathbb{R}^3$ is the angular velocity, $h_{\text{RW}} \in \mathbb{R}^3$ and τ_{RW} are the angular momentum of RW and torque.

ACKNOWLEDGMENT

This work was partially supported by the JAXA, Space Strategy Fund GRANT Number (JPJXSSF24MS09003), Japan. The first author would like to thank Yoichi Tomioka at the University of Aizu for technical discussion and Atsuki Ochi at Interstellar Technologies Inc. for controller gain tuning.

REFERENCES

- [1] S. R. Khan, S. K. Pavuluri, and M. P. Desmulliez, "Accurate modeling of coil inductance for near-field wireless power transfer," *IEEE Transactions on Microwave Theory and Techniques*, vol. 66, no. 9, pp. 4158–4169, 2018.
- [2] L. I. N. de Lara, M. Daneshzand, A. Mascarenas, D. Paulson, K. Pratt, Y. Okada, T. Raij, S. N. Makarov, and A. Nummenmaa, "A 3-axis coil design for multichannel tms arrays," *Neuroimage*, vol. 224, p. 117355, 2021.
- [3] Q. Ze, S. Wu, J. Nishikawa, J. Dai, Y. Sun, S. Leanza, C. Zemelka, L. S. Novelino, G. H. Paulino, and R. R. Zhao, "Soft robotic origami crawler," *Science Advances*, vol. 8, no. 13, p. eabm7834, 2022.
- [4] T. Shibata and S.-I. Sakai, "A contactless micro-vibration isolator using the flux pinning effect for space telescopes," *Journal of Spacecraft and Rockets*, vol. 59, no. 2, pp. 651–659, 2022.
- [5] E. Fabacher, S. Lizy-Destrez, D. Alazard, F. Ankersen, and A. Profizi, "Guidance of magnetic space tug," *Advances in Space Research*, vol. 60, no. 1, pp. 14–27, 2017.
- [6] Y. Takahashi, S. Shim, and S.-i. Sakai, "Distance-based relative orbital transition for palm-sized satellite swarm with guaranteed escape-avoidance," in *AIAA Scitech 2025 Forum*, 2025, p. 2068.
- [7] R. C. Foust, E. S. Lupu, Y. K. Nakka, S.-J. Chung, and F. Y. Hadaegh, "Ultra-soft electromagnetic docking with applications to in-orbit assembly," in *69th International Astronautical Congress, Bremen, Germany*, 2018, pp. 1–5.
- [8] H. Tajima, Y. Takahashi, T. Shibata, H. Sakamoto, and S.-i. Sakai, "Study on short range formation flight and docking control using ac magnetic field," in *74th International Astronautical Congress, Baku, Azerbaijan*, 2-6 October 2023. [Online]. Available: <https://iafaastro.directory/iaac/archive/browse/IAC-23/C1/IPB/77992/>
- [9] A. K. Porter, D. J. Alinger, R. J. Sedwick, J. Merk, R. A. Opperman, A. Buck, G. Eslinger, P. Fisher, D. W. Miller, and E. Bou, "Demonstration of electromagnetic formation flight and wireless power transfer," *Journal of Spacecraft and Rockets*, vol. 51, no. 6, pp. 1914–1923, 2014.
- [10] Y. Takahashi, S. Seang, S. Yusuke, Y. Hideki, I. Masaru, I. Norit-suna, M. Sumio, S. Shin-Ichiro, and I. Takahiro, "Experimental study of magnetically-actuated satellite swarm: Controllability extension via time-integrated control with geometry learning," in *SMC-IT/SCC 2025 Space Robotics Workshop*. IEEE, 2025.
- [11] S. A. Schweighart, "Electromagnetic formation flight dipole solution planning," Ph.D. dissertation, Massachusetts Institute of Technology, 2005. [Online]. Available: <http://hdl.handle.net/1721.1/32464>
- [12] Y. Takahashi, H. Sakamoto, and S.-i. Sakai, "Kinematics control of electromagnetic formation flight using angular-momentum conservation constraint," *Journal of Guidance, Control, and Dynamics*, vol. 45, no. 2, pp. 280–295, 2022.
- [13] Y. Takahashi, A. Ochi, Y. Tomioka, and S.-I. Sakai, "Noda-mmh: Certified learning-aided nonlinear control for magnetically-actuated swarm experiment toward on-orbit proof," in *International Conference on Space Robotics 2025*. IEEE, 2025.
- [14] Z. Abbasi, J. B. Hoagg, and T. M. Seigler, "Decentralized electromagnetic formation flight using alternating magnetic field forces," *IEEE Transactions on Control Systems Technology*, vol. 30, no. 6, pp. 2480–2489, 2022.
- [15] Y. Takahashi, "Neural power-optimal magnetorquer solution for multi-agent formation and attitude control," *arXiv preprint*, 2024.
- [16] S. Shim, Y. Takahashi, N. Usami, M. Kubota, and S.-i. Sakai, "Feasibility analysis of distributed space antennas using electromagnetic formation flight," in *2025 IEEE Aerospace Conference*, 2025, pp. 1–18.
- [17] T. Miyato, T. Kataoka, M. Koyama, and Y. Yoshida, "Spectral normalization for generative adversarial networks," *arXiv preprint arXiv:1802.05957*, 2018.
- [18] D. P. Kingma, "Adam: A method for stochastic optimization," *arXiv preprint arXiv:1412.6980*, 2014.
- [19] G. Shi, X. Shi, M. O'Connell, R. Yu, K. Azizzadenesheli, A. Anandkumar, Y. Yue, and S.-J. Chung, "Neural lander: Stable drone landing control using learned dynamics," in *2019 International Conference on Robotics and Automation (ICRA)*. IEEE, 2019, pp. 9784–9790.